Physics in Medicine & Biology

IPEM Institute of Physics and Engineering in Medicine

ACCEPTED MANUSCRIPT • OPEN ACCESS

Enabling non-isocentric dynamic trajectory radiotherapy by integration of dynamic table translations

To cite this article before publication: Gian Guyer *et al* 2022 *Phys. Med. Biol.* in press https://doi.org/10.1088/1361-6560/ac840d

Enabling non-isocentric dynamic trajectory radiotherapy by integration of dynamic table translations

G Guyer, S Mueller, C Koechli, D Frei, W Volken, J Bertholet, P-H Mackeprang, H A Loebner, D M Aebersold, P Manser and M K Fix

Division of Medical Radiation Physics and Department of Radiation Oncology, Inselspital, Bern University Hospital, and University of Bern, 3010 Bern, Switzerland

E-mail: gian.guyer@insel.ch

January 2022

Abstract.

Objective: The purpose of this study is to develop a treatment planning process (TPP) for non-isocentric dynamic trajectory radiotherapy (DTRT) using dynamic gantry rotation, collimator rotation, table rotation, longitudinal, vertical and lateral table translations and intensity modulation and to validate the dosimetric accuracy.

Approach: The TPP consists of two steps. First, a path describing the dynamic gantry rotation, collimator rotation and dynamic table rotation and translations is determined. Second, an optimization of the intensity modulation along the path is performed. We demonstrate the TPP for three use cases. First, a non-isocentric DTRT plan for a brain case is compared to an isocentric DTRT plan in terms of dosimetric plan quality and delivery time. Second, a non-isocentric DTRT plan for a craniospinal irradiation (CSI) case is compared to a multi-isocentric intensity modulated radiotherapy (IMRT) plan. Third, a non-isocentric DTRT plan for a bilateral breast case is compared to a multi-isocentric volumetric modulated arc therapy (VMAT) plan. The non-isocentric DTRT plans are delivered on a TrueBeam in developer mode and their dosimetric accuracy is validated using radiochromic films.

Main results: The non-isocentric DTRT plan for the brain case is similar in dosimetric plan quality and delivery time to the isocentric DTRT plan but is expected to reduce the risk of collisions. The DTRT plan for the CSI case shows similar dosimetric plan quality while reducing the delivery time by 45% in comparison with the IMRT plan. The DTRT plan for the breast case showed better treatment plan quality in comparison with the VMAT plan. The gamma passing rates between the measured and calculated dose distributions are higher than 95% for all three plans.

Significance: The versatile benefits of non-isocentric DTRT are demonstrated with three use cases, namely reduction of collision risk, reduced setup and delivery time and improved dosimetric plan quality.

Keywords: Dynamic Trajectory Radiotherapy, Direct aperture optimization, Multi-isocentric treatment techniques

Submitted to: *Phys. Med. Biol.*

1. Introduction

Modern radiotherapy aims at delivering highly conformal dose distributions to the tumor while sparing the surrounding normal tissue. The introduction of intensity modulated radiotherapy (IMRT) utilizing the multileaf collimator (MLC) improved target conformality in comparison with 3D conformal radiotherapy (Bortfeld 2006). Volumetric modulated arc therapy (VMAT) improved upon the delivery efficiency of IMRT while maintaining the dosimetric treatment plan quality by rotating the gantry continuously during beam on (Otto 2008). Both VMAT and IMRT are established treatment techniques in radiotherapy for more than a decade.

Next to the MLC, current linear accelerators offer additional degrees of freedom (DoFs) applicable to improve upon VMAT and IMRT in terms of dosimetric treatment plan quality, delivery efficiency or patient safety. By rotating the patient table between the delivery of different beams, non-coplanar beam directions can be achieved to further improve organ-at-risk (OAR) sparing either for IMRT (Dong et al. 2013, Rwigema et al. 2015, Yu et al. 2018) or for VMAT (Audet et al. 2011, Clark et al. 2012). In a more advanced technique, the table is rotated simultaneously with the gantry during beam on (Smyth et al. 2013, MacDonald and Thomas 2015, Papp et al. 2015, Wild et al. 2015, Lyu et al. 2018, Mullins et al. 2020a). In dynamic trajectory radiotherapy (DTRT), the collimator is rotated additionally to the gantry and table, yielding a further DoF (Yang et al. 2011, Fix et al. 2018, Langhans et al. 2018, Dong et al. 2018, MacDonald et al. 2020). Dynamic collimator rotations enable connectedness improvements between MLC apertures (Locke and Bush 2017). In addition, the whitespace inside the open MLC area is reduced, which is especially relevant for treating multiple targets (MacDonald et al. 2018, Battinelli et al. 2021). High dosimetric accuracy of DTRT has been shown in the past (Smyth et al. 2019a, Manser et al. 2019). A review of non-coplanar radiotherapy techniques is given by Smyth et al. (2019b).

Currently, DTRT is limited to fixed isocenter positions. This could be extended to a non-isocentric technique utilizing the translational DoFs offered by modern patient tables in longitudinal, vertical and lateral direction (Schmidhalter et al. 2014), resulting in an even more general trajectory for DTRT (Manser et al. 2020). One potential use case of non-isocentric DTRT, i.e. DTRT including dynamic table translations, is to extend the source-target distance (STD) for VMAT and DTRT plans. This is achieved by defining a virtual isocenter (Humm 1994) given by the position of the machine isocenter in the isocentric VMAT or DTRT plan inside the patient. The STD can thus be extended by moving the table such that the virtual isocenter is moved further away from the source in beam direction in comparison to the actual machine isocenter. With extended STD, the risk of collision between gantry and patient is reduced, e.g. for targets positioned laterally in the body, and at the same time the solution space could be expanded by avoiding collisions between gantry and table (Yu et al. 2015, Liang et al. 2015, Yu et al. 2018). Another possible use case is the dynamic translation similar to helical VMAT (Bedford et al. 2012) to irradiate large targets such as craniospinal irradiation (CSI)

for pediatric brain tumors (Laprie et al. 2015, Massimino et al. 2016) or leptomeningeal disease (Maillie et al. 2021), which is commonly performed with a multi-isocenter proton or photon technique (Seravalli et al. 2018), with e.g. 2-3 isocenters. A third possible use case is to exploit dynamic table translation for concave targets such as whole breast irradiation (WBI) in order to use more tangential beam directions in comparison with a single isocenter technique (Li et al. 2014).

Non-isocentric DTRT requires a treatment planning process (TPP) which is able to handle all the dynamic axes appropriately. To the best of our knowledge, no optimization algorithm has been described in literature, which can perform intensity modulation optimization along any predefined path including dynamic table translation. Mullins et al. (2020a) proposed a TPP for DTRT plans with a predefined, non-isocentric trajectory for cranial targets at a shortened STD. However, the proposed TPP is not able to handle arbitrary non-isocentric dynamic trajectories.

A possibility is to extend an existing isocentric DTRT intensity modulation optimization algorithm to non-isocentic DTRT. In our group, a two-step planning technique for isocentric DTRT was developed in previous work, where in a first step the path describing the dynamic gantry, collimator and table rotation is determined and in a second step, intensity modulation is performed (Fix et al. 2018). However, the intensity modulation optimization is done within a commercial treatment planning system, which is not able to handle dynamic table translations.

The purpose of this work is to develop a TPP for DTRT using dynamic axes, that is rotating gantry and rotating collimator, rotating and translating table and intensity modulation during beam on. For this, intensity modulation optimization of DTRT plans is enabled in an in-house DAO algorithm. Three clinically motivated cases are used to investigate potential use cases for non-isocentric DTRT. Furthermore, the deliverability of non-isocentric DTRT plans is shown on a TrueBeam linear accelerator (Varian Medical Systems, Palo Alto, CA) in developer mode and dosimetric accuracy is demonstrated using radiochromic film measurements.

2. Methods

2.1. Treatment planning process

In the following section, the TPP for non-isocentric DTRT is described in detail. The TPP consists of two main parts. First, determination of the dynamic path, which is given by a set of control points (CPs) defining the dynamic axes, that is gantry rotation, collimator rotation, table rotation and longitudinal, lateral and vertical table translation. If an axis has a constant value for all CPs, it is called a static axis in the following. Second, optimization of the intensity modulation is performed by setting the MLC sequence and corresponding MU weights for each CP. The TPP is described for DTRT plans, but also works for VMAT as VMAT is a special case of DTRT with static table and collimator.

2.1.1. Path determination Planning CTs and structure sets were taken from cases previously treated at our institution and imported into a research version of the Eclipse treatment planning system (TPS) 15.6 (Varian Medical Systems, Palo Alto, CA). A normal tissue structure was created, defined as the body contour excluding the planning target volume (PTV). The paths are determined by using one of two different Eclipse TPS interfaced scripts. In the following, the two different scripts for path determination are described:

(i) Manual path generation. For this, anchor points are defined in a list by the user by setting values for gantry angle, collimator angle, table angle and lateral, vertical and longitudinal table position. Using these anchor points, the CPs are obtained by linearly interpolating between two consecutive anchor points in the list with a given spacing in each axis, resulting in the definition of the path. This can be used for VMAT and DTRT. In the case of VMAT, two anchor points are used for start and end point of the arc with a static table position and collimator angle. Multiple paths are obtained by starting the script multiple times.

(ii) Path determination as described in Fix et al. (2018) for isocentric DTRT. In brief, in this approach, the gantry, collimator and table angles are optimized using mainly a geometrical approach. A map based on volumetric target/OAR overlap in beam's eye view is created. On this map, the gantry-table path is determined using an A* algorithm (Hart et al. 1968). For the collimator rotation along the gantry-table path, a map is created scoring different gantry-collimator combinations by the distance between the outer most MLC leaf positions when the MLC is set conformal. Then, the gantry-collimator path is determined by finding the collimator rotation for which this distance is minimal.

For both options, the STD can be changed from the conventional 100 cm to a value d in a post-processing step by moving the virtual isocenter further away in beam direction using the following trigonometric calculations:

$$\Delta_{lateral} = (d - 100\ cm) \cdot \sin(-\alpha_{gantry}) \cdot \cos(\alpha_{table}) \quad (1)$$

$$\Delta_{vertical} = (d - 100\ cm) \cdot \cos(\alpha_{gantry}) \quad (2)$$

$$\Delta_{longitudinal} = (d - 100\ cm) \cdot \sin(-\alpha_{gantry}) \cdot \sin(\alpha_{table}), \quad (3)$$

where α_{gantry} and α_{table} are the gantry and table angles, respectively, and $\Delta_{lateral}$, $\Delta_{vertical}$ and $\Delta_{longitudinal}$ are the lateral, vertical and longitudinal table positions relative to the table position in the isocentric DTRT.

Next, the field size defined by the secondary collimator jaws is set to the smallest possible opening such that the PTV with an additional 5 mm margin is not blocked by the jaws for any CPs from the beam's-eye-view or set to the largest possible size in the case where the PTV is larger than the largest possible field size, e.g. in CSI.

2.1.2. Intensity modulation optimization To provide the necessary dosimetric information for the intensity modulation optimization, a beamlet dose calculation is

performed using the Eclipse TPS interfaced Swiss Monte Carlo Plan (SMCP) (Fix et al. 2007) for each CP after the path generation. The beamlet grid is set up for each CP with the grid spacing given by the width of the MLC leaves in transverse direction and 5 mm in direction of MLC leaf movement and the grid size equivalent to the field size rounded to the next beamlet border. A precalculated phase space at the exit of the treatment head, used as an input the VMC++ dose calculation algorithm (Kawrakow and Fippel 2000) are used to calculate the beamlet dose distributions for each CP.

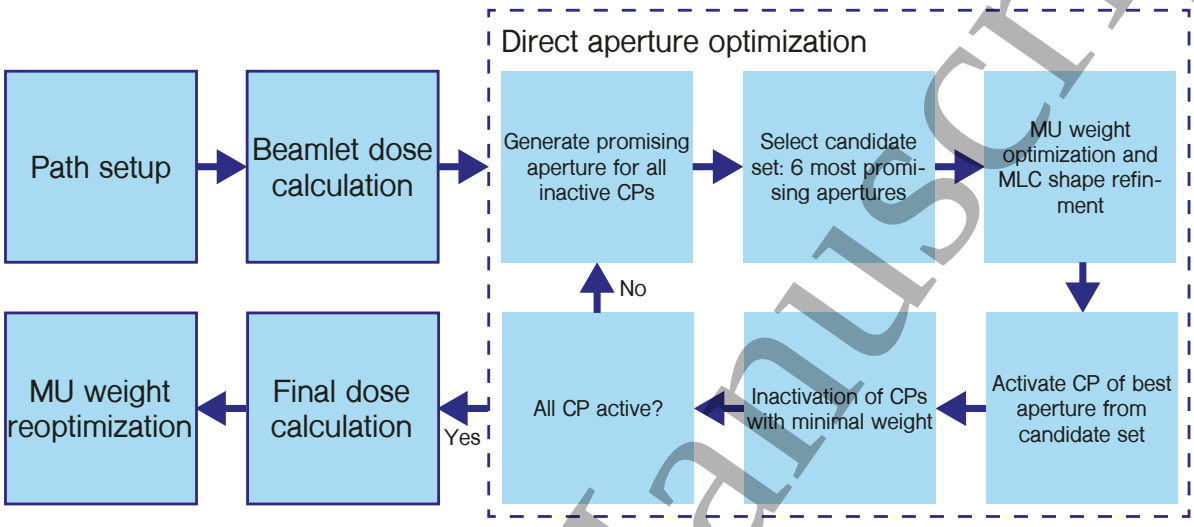

Figure 1. Overview of the intensity modulation optimization steps. After the path setup, a beamlet dose calculation is performed for all CPs. Next, an aperture is determined for all CPs using a direct aperture optimization by iteratively adding apertures to CPs, i.e. activating the CPs. For this, a promising aperture is determined for all inactive CPs. Out of these, the six most promising apertures are selected, i.e. those with the steepest gradient on the objective function value. Each CP of these six apertures is activated individually and a MU weight optimization and MLC shape refinement is performed together with all active CPs. Next, the best aperture out of the six most promising ones is identified based on the objective function value. Afterwards, some active CPs are allowed to be inactivated if their MU weight is below a minimal value and if the total number of inactivated CPs in the optimization is not higher than a selected threshold. When all CPs are activated, a final dose calculation and a MU weight reoptimization are performed.

Using the beamlet dose distributions, the intensity modulation is optimized with inverse planning by determining exactly one aperture, i.e. the MLC shape and the corresponding MU weight, at each CP. The intensity modulation optimization algorithm is an extension of the hybrid DAO algorithm and based on column generation (CG) and simulated annealing (SA) described by Mueller et al. (2022). The objective function is evaluated on a plan dose D_{plan}, which is given by the following equation:

$$D_{plan} = \sum_{n=1}^{\#CPs} \sum_{j=1}^{\#leafpairs} \sum_{b=1}^{\#beamlets} D_n(b,j) \cdot w_n \cdot \phi_n(b,j), \tag{4}$$

where $D_n(b,j)$ is the dose of beamlet b and leaf pair j at the nth CP, w_n is the MU weight of the aperture at the nth CP and $\phi_n(b,j)$ is the fluence of the beamlet b and

leaf pair j of the aperture at the nth CP. An overview of the optimization is given in figure 1. The optimization starts with each CP having an undetermined aperture and w_n set to 0, called an inactive CP. In every iteration, one CP is set to active by determining the corresponding aperture, i.e. the MLC leaf pattern and MU weight w_n. For this, a promising aperture, i.e. the aperture with the lowest price on the gradient objective function value of each beamlet belonging to the aperture summed together, is determined for each inactive CP.

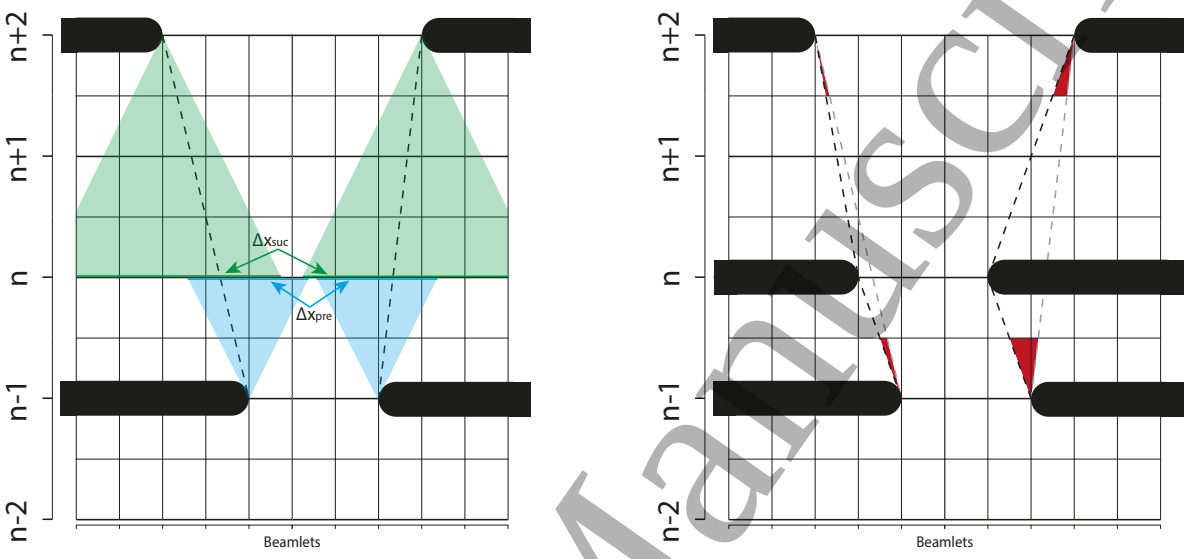

(a) Before (b) After

Figure 2. Illustration of the fluence interpolation for one MLC leaf pair. (a) Situation before the leaf pair at the nth CP is inserted. The leaf motion is interpolated between the next active CPs $n-1$ and $n+2$. The MLC preceding $\Delta x_{pre}(n)$ and succeeding $\Delta x_{suc}(n)$ ranges are illustrated in blue and green. The position of the leaf pair at the nth CP is restricted to the intersection of these ranges. (b) Situation after the leaf pair at n is inserted. The black dashed lines represent the interpolated leaf motion and the red areas correspond to the change in fluence of the neighboring apertures due to the insertion of a new leaf pair.

In the determination of these promising apertures, the maximum distance the MLC is allowed to travel between neighboring CPs is steered with Δx ranges for each leaf. For a new promising aperture at the nth CP, the MLC range is determined with the next preceding and succeeding active CPs, as illustrated in figure 2(a). For an already preceding active CP at $(n-q)$, the MLC $\Delta x_{pre}(n)$ range is given by

$$\Delta x_{pre}(n) = \lambda_{MLC} \cdot v_{MLC} \cdot \sum_{i=n-q}^{n-1} t(i), \tag{5}$$

where v_{MLC} is the maximal mechanical MLC leaf speed, $t(i)$ is the time needed to move all the dynamic axes from the ith CP to the $(i+1)$th CP and λ_{MLC} is the so-called MLC freedom factor, which is a parameter defining how much the MLC is allowed to

slow down the delivery. If λ_{MLC} is equal to 1, the MLC range is limited such that the time needed for the MLC leaves to move is not longer than the time needed to move the dynamic axes between CPs. If λ_{MLC} is equal to 2, the time needed for moving the MLC leaves can be at most two times longer than the maximal time needed to move all the dynamic axes and consequently delivery time can be up to doubled. If λ_{MLC} is smaller than 1, the range is restricted further but without an impact on the delivery time because the MLC leaf travel is not the limiting motion. The allowed $\Delta x_{suc}(n)$ range is calculated similarly if there is a succeeding active CP.

The time $t(i)$ in (5) is calculated by

$$t(i) = \max_a \Big((x_a(i+1) - x_a(i))/v_a \Big), \tag{6}$$

where $x_a(i)$ is the position of the axis a at the ith CP and v_a is the maximal mechanical speed limit of axis a with $a \in$ {gantry rotation, collimator rotation, table rotation, longitudinal table translation, vertical table translation, lateral table translation}. The values used for v_a are given in table 1.

Among all the promising apertures, the one which leads to the largest decrease of the objective function is determined. For this, the six most promising apertures with the lowest price are identified. This is done for the six most promising instead of all promising apertures to keep computational efficiency reasonable for dynamic plans which have typically over 100 CPs and the number of six has proven to be an adequate number in preliminary investigations. Each CP of the six promising apertures is set separately to active and a suboptimization is performed with all active CPs including one CP of the six promising apertures. The suboptimization consists of an MU weight optimization of the active CPs using an L-BFGS quasi newton method (Nocedal and Wright 1999). Subsequently, the aperture shapes and weights of the active CPs are refined using a stochastic SA algorithm, where either an MLC leaf or the MU weight of a CP is selected and tested for potential improvement in each iteration. The MLC leaf positions are restricted by the maximal MLC range given by (5). The SA algorithm is followed by a second MU weight optimization of the CPs. The MU weights of the active CPs are limited to a maximal value given by

$$w_{max} = \lambda_{MU} \cdot r_{max} \cdot t_n, \tag{7}$$

where r_{max} is the maximal MU rate of the beam, λ_{MU} is the so-called MU freedom factor and t_n is the time associated with CP n, which is calculated by

$$t_n = \frac{1}{2} \cdot t(n-1) + \frac{1}{2} \cdot t(n), \tag{8}$$

where $t(i)$ is given by (6). Like the MLC freedom factor, the maximal time needed for delivering the MUs is equal or lower than the time needed to move all dynamic axes if λ_{MU} is set to 1. To prevent a beam hold due to a too low MU rate during the delivery, the MU weights are also limited by a minimal value

$$w_{min} = r_{min} \cdot t_n, \tag{9}$$

where r_{min} is the minimal MU rate such that no beam hold occurs. During dose delivery of trajectories with dynamic axes, the MLC leaves move continuously from the aperture of one CP to the next CP simultaneously with the dynamic axes. Thus, when a promising aperture at a CP is determined or the aperture shape at an active CP is changed, the fluence associated with this aperture is dependent on the shape of the neighboring apertures. This is taken into account by interpolating the fluence to the neighboring apertures. The fluence of the neighboring apertures is recalculated using the same formalism to respect the influence of changes on the neighboring apertures, as illustrated in figure 2(b). Note that due to the influence of changes on the neighboring apertures, the optimization problem is considerably more complicated when considering fluence interpolation in comparison to optimization without fluence interpolation. The fluence interpolation is considered both in the pricing of promising apertures as well as calculating the objective function value and gradient of the active CPs. The full formalism of fluence interpolation is described in Appendix A.

After the suboptimization, the aperture among the six most promising apertures is identified, for which the suboptimization together with all apertures of active CPs yielded the lowest objective function value. The CP of this promising aperture is set to active, while all other promising apertures are removed. If the MU weight of an active CP is set to the minimal weight in one iteration, the CP is inactivated to allow for a better aperture shape at this CP at a later iteration. The total number of active CPs which can be inactivated in all iterations summed together is limited to 33% of the number of CPs to guarantee that the optimization reaches an end and for computational efficiency reasons. This threshold was determined in preliminary investigations showing that higher percentages only increase the computational time without having an impact on the optimization result. If this number is reached, no further CPs are inactivated. The optimization is terminated when every CP is active.

As mentioned, the beamlet dose calculations are performed for the discrete set of CPs. However, the delivery of the beam is not done from the discrete set of CPs, but by simultaneous continuous movement of the MLC and dynamic axes between CPs. Thus, the summed beamlet dose after the optimization and the actual dose delivered to the patient differ. Additionally, the transmission through the MLC leaves and contributions from scatter considered during optimization are only an approximation. Hence, a final dose calculation taking the continuous movement and the exact MLC geometry into account is performed. A Monte Carlo (MC) dose calculation algorithm is favorable over other calculation algorithms for this task, because the simulated particles can be continuously sampled from all positions of the continuously moving and changing aperture (Manser et al. 2019). The MC dose calculation is performed using the SMCP integrated beam model (Magaddino et al. 2011) and VMC++ dose calculation algorithm (Kawrakow and Fippel 2000). A voxel size of $2.5 \times 2.5 \times 2.5$ mm^3 is used for all MC dose calculations and the actual mean statistical uncertainty of the voxels with dose values higher than 50% of the maximum dose calculated is below 0.5% for all presented dose distributions.

To mitigate the difference between the optimized beamlet dose and final dose calculation, a reoptimization of the MU weights of the CPs is performed after the final dose calculation. The MU weight reoptimization is done with an L-BFGS algorithm while considering the limitations on the MU weights from the optimization. After the reoptimization, the dose distribution of each aperture is weighted with the reoptimized MUs and summed to obtain the reoptimized final dose distribution of the plan. Some investigations of the optimization efficacy are given in Appendix B.

2.2. Use cases

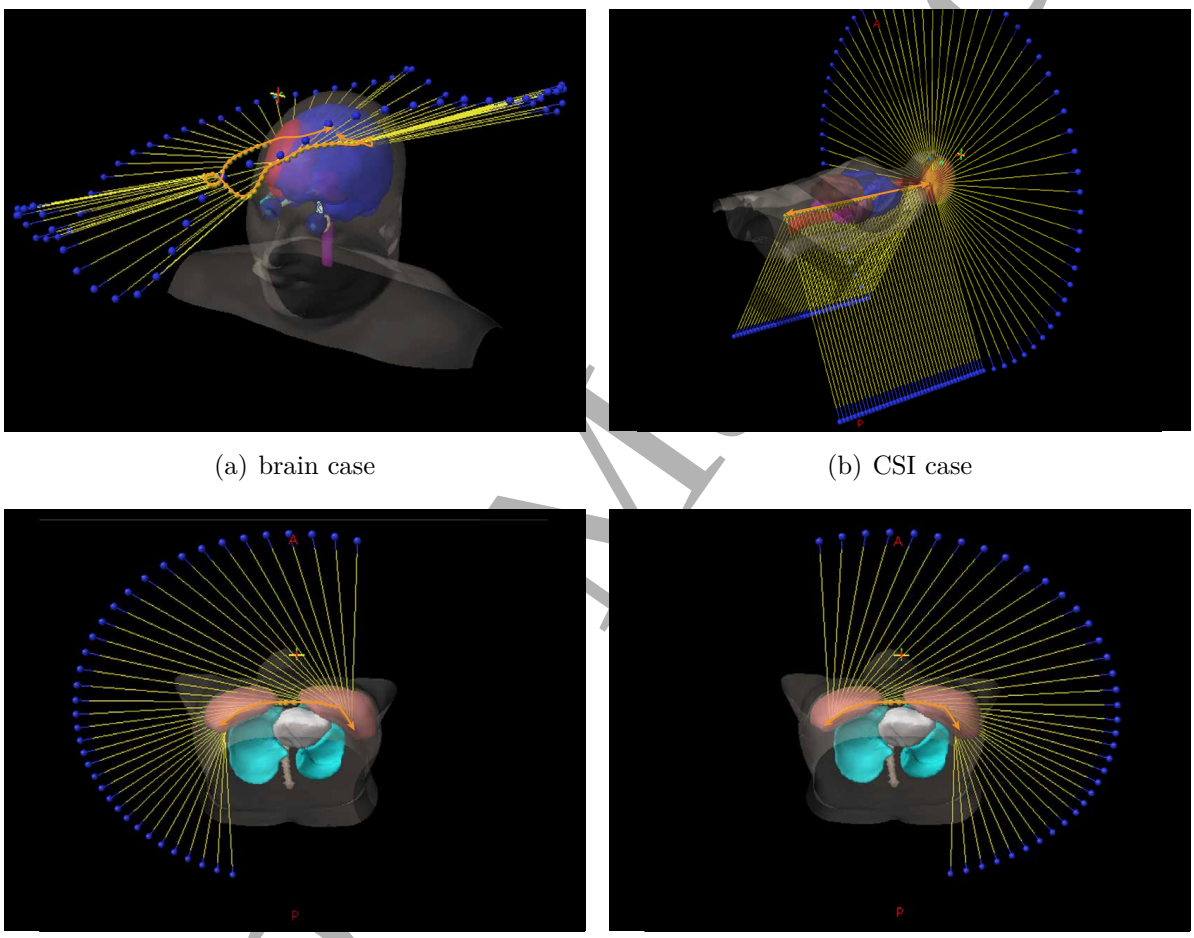

(a) brain case (b) CSI case

(c) WBI case A (d) WBI case B

Figure 3. Illustrations of the paths in Eclipse TPS for the DTRT plan with extended STD for the brain case (top left), the DTRT plan for the CSI case (top right) and the DTRT plan for the WBI case (bottom). The paths are given by a set of CPs defining the gantry rotation, collimator rotation and table rotation and translation. For better visibility, only the central axis of the beam at each CPs is shown as yellow lines. The position of the machine isocenter in the patient coordinate system is illustrated in orange.

As a first use case, non-isocentric DTRT with an extended STD is considered. For

Table 1. Values used for time calculation.

Axis a	Speed limit v_a
Gantry rotation	6°/s
Collimator rotation	15°/s
Table rotation	3°/s
Longitudinal table translation	8 cm/s
Vertical table translation	2 cm/s
Lateral table translation	4 cm/s
Max. dose rate	600 MU/min
Min. dose rate	5 MU/min
MLC leaf movement	2.5 cm/s

this, a DTRT plan with extended STD of 110 cm for a brain case with a prescribed dose of 60 Gy to the median dose of the PTV in 30 fractions is compared in terms of dosimetric quantities and estimated delivery time to a plan with the same DTRT path but with normal STD of 100 cm, i.e. an isocentric plan. The gantry-table and gantry-collimator path is determined by the method described by Fix et al. (2018). The resulting path is duplicated into two paths. The spacing between CPs is 5° based on the gantry angle value. In figure 3(a), the path of the DTRT plan with extended STD is illustrated. The parameters used for the optimization are $\lambda_{MU} = 2$, $\lambda_{MLC} = 1$ and with fluence interpolation applied.

The dosimetric quantities used are $D_{2\%}$ for serial OARs, D_{mean} for parallel OARs, $V_{10\%}$ for normal tissue and homogeneity index (HI) for the PTV

$$\mathrm{HI} = (D_{2\%} - D_{98\%})/D_p, \tag{10}$$

where D_p is the prescribed dose. The estimated delivery time is calculated by summing the time per CPs of all trajectories, as well as the time to move axes between fields, if necessary. The time per CP is estimated using (6) with the MLC leaf travel and the MU weight as additional components. In this formula, the acceleration of the mechanical axes as well as the beam ramp up are neglected. The mechanical speed limits v_a used for the calculation are shown in table 1.

As a second use case, a CSI case with a prescribed median dose of 23.4 Gy to the PTV in 13 fractions is considered. A DTRT plan is created consisting of a 70 cm longitudinal table translation along the spinal axis with a static gantry angle of −150°, a gantry rotation around the head and another 70 cm longitudinal table translation with a gantry angle of 150°. The spacing of CPs is set to 2 cm along the longitudinal table axis and 5° along the gantry rotation. The path of the DTRT plan is illustrated in figure 3(b). The path is duplicated and the intensity optimization is performed using $\lambda_{MU} = 2$, $\lambda_{MLC} = 1$ and with fluence interpolation applied. The resulting DTRT plan is compared to an IMRT plan consisting of six fields, four dorsal angulated fields

for the spinal axis and two lateral fields for the brain, separated in three isocenters, which corresponds to the field setup used in the original clinical plan. The number of total apertures of the IMRT plan is set to 30, because investigations for this field setup showed that additional apertures improve the dosimetric plan quality only marginally. The plans are compared in terms of estimated delivery time and dosimetric quantities.

As a third use case, a non-isocentric DTRT plan for a bilateral WBI case with a prescribed median dose of 50 Gy to the PTV in 25 fractions is compared to a VMAT plan in terms of dosimetric treatment plan quality and delivery time. The non-isocentric DTRT setup consists of half arcs with dynamic vertical and lateral table translation such that the central beam axis stays tangential to the body contour. In figure 3(c) and 3(d) the DTRT paths are illustrated. Each of the two paths is duplicated for a total of four half arcs. The VMAT setup consists of 12 partial arcs in two isocenters, which corresponds to the clinical field setup. For the right breast, two arcs range from $-180°$ to $-115°$ in gantry angle, two arcs range from $-180°$ to $45°$ and two range from $-20°$ to $60°$. For the left breast, the gantry angles range from $-60°$ to $20°$, from $-45°$ to $180°$ and from $115°$ to $180°$ for two arcs each. For both the DTRT and the VMAT setup, the spacing between CPs is $5°$ based on the gantry angle value and the parameters used for the optimization are $\lambda_{MU} = 2$, $\lambda_{MLC} = 1$ and with fluence interpolation applied. All optimizations are calculated on an AMD Epyc2 processor using six CPU cores.

2.3. Validation

To validate the TPP for non-isocentric DTRT, the plan with extended STD of the brain case, the DTRT plan of the CSI case and the DTRT plan of the WBI case are delivered on a TrueBeam linear accelerator in developer mode. The dose is measured using two interleaved radiochromic EBT3 films (Ashland Advanced Materials, Bridgewater, NJ) placed inside a PMMA cube. The PMMA cube is made of an outer case with four blocks inside. This phantom allows to put the EBT3 films in the middle of the blocks and between the blocks and the outer case of the cube in the axial, sagittal and coronal plane of a patient lying on the treatment table. An image of the measurement setup as well as an illustration of the PMMA cube including proportions is shown in figure 4. For the plans of the brain and CSI case, the films are placed in the middle of the cube in the sagittal and coronal plane while for the plan of the WBI case one film is placed in the middle in the axial plane and one film is placed on a coronal plane in a depth of 2 cm, i.e. between the outer case and the inner blocks. Because the target of the CSI case is too long to fit into the PMMA cube, the neck region is chosen for measurement to incorporate both the longitudinal table translation and the gantry arc into the measurement. The films are scanned using an Epson XL 10000 flatbed scanner (Seiko Epson Co., Tokyo, Japan) 18h after irradiation. The scanned films are corrected for the lateral response artifact of the scanner using a one-dimensional linear correction function (Lewis and Chan 2015). The color values on the films are converted to absolute dose using a triple channel calibration (Micke et al. 2011) and

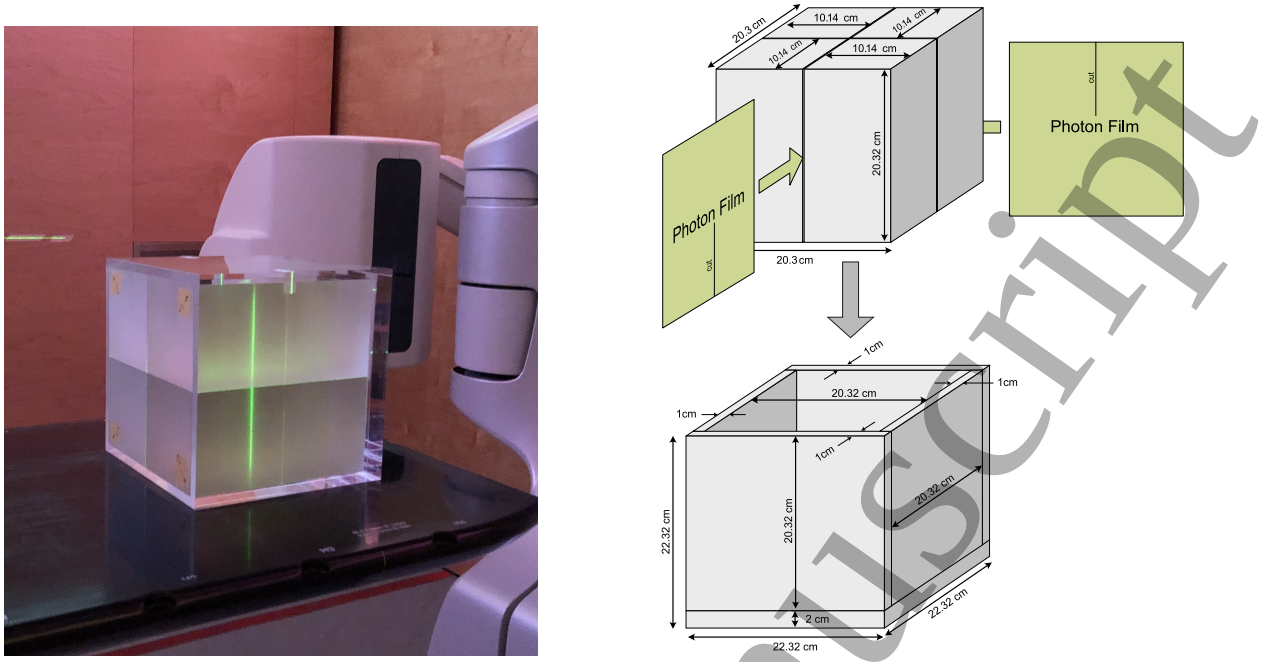

(a) (b)

Figure 4. Photo and illustration of the PMMA cube used for the validation measurements. Two EBT3 films, one in the sagittal and one in the coronal plane are placed inside the cube.

rescaled according to the one-scan protocol by using two additional film strips (Lewis et al. 2012). The resulting dose of the red channel is compared to the corresponding 2D plane of the dose recalculated for the PMMA cube using a gamma evaluation with a 3% (global) / 2 mm and a 2% (global) / 2 mm criterion and a 10% low-dose threshold of the maximum dose.

3. Results

3.1. Treatment quality of use cases

In figure 5 the values of the dynamic axes are shown for the first trajectory of the DTRT plan with extended STD for the brain case. As can be seen, the gantry, collimator and table dynamically rotate and the table dynamically translates in all three directions during the trajectory. In figure 6 the DVH comparison of the brain case DTRT plans with extended vs. normal STD is shown. The DVHs of the PTV, OARs and normal tissue of the two plans are similar. The estimated delivery time is 3.4 min for the plan with normal STD and 3.5 min for extended STD. The total number of MUs are 550 and 610 for normal and extended STD plans, respectively.

Figure 7 shows the DVH comparison between the DTRT plan and the IMRT plan for the CSI case. The dosimetric quantities are compared in table 2. The plan quality is similar between the two plans. The estimated delivery time is 4.6 min for the DTRT

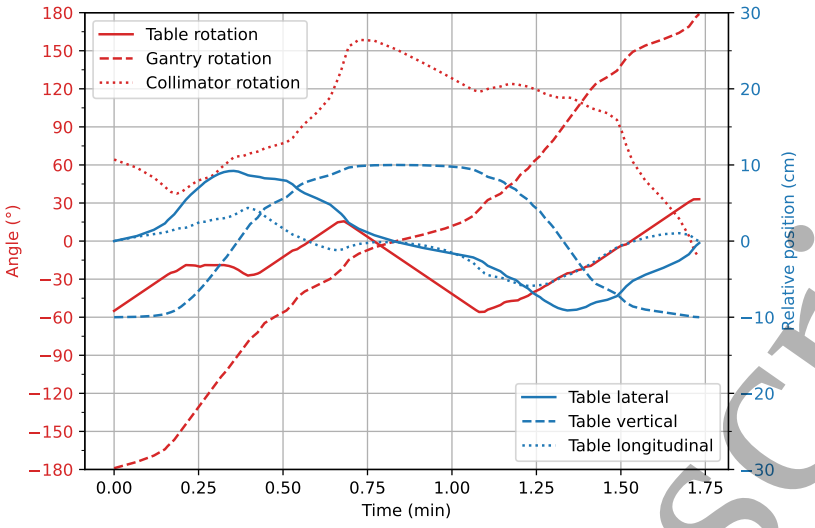

Figure 5. Gantry, collimator and table values for first trajectory of the DTRT plan with extended STD for the brain case.

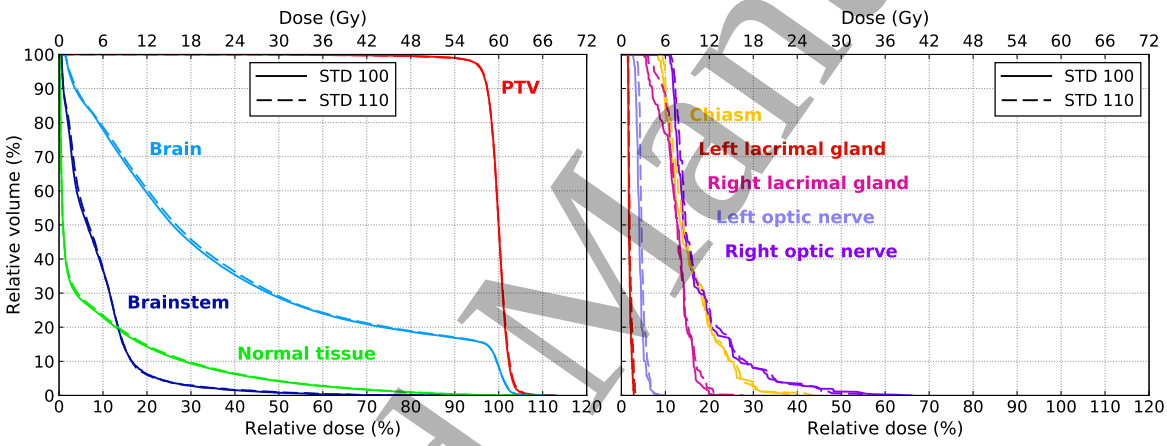

Figure 6. DVH comparison of the DTRT plan with extended STD (110 cm) and isocentric DTRT plan (100 cm) for the brain case.

plan and 8.3 min for the IMRT plan. The total number of MUs are 1145 for the DTRT plan and 764 for the IMRT plan.

In figure 8(a) and figure 8(b) the doses of the DTRT and IMRT plans for the CSI case are visualized in a sagittal plane and in figure 8(c) dose profiles are shown for the fields of the IMRT and DTRT plans. Due to the longitudinal table translation, there are no field junctions as in the multi-isocentric IMRT plan.

The results for the WBI case are shown in figures 9 and 10. As can be seen in the DVHs in figure 9, the HI is similar between the VMAT and the DTRT plan. However, the mean heart dose is 6.6 Gy in the VMAT plan and 3.9 Gy in the DTRT plan, which corresponds to a 40% reduction. In addition, the total lung volume receiving at least 5 Gy is 90% in the VMAT plan and 29% in the DTRT plan, which corresponds to a reduction of 67%. In figure 10, the dose distributions of the VMAT and DTRT plans of

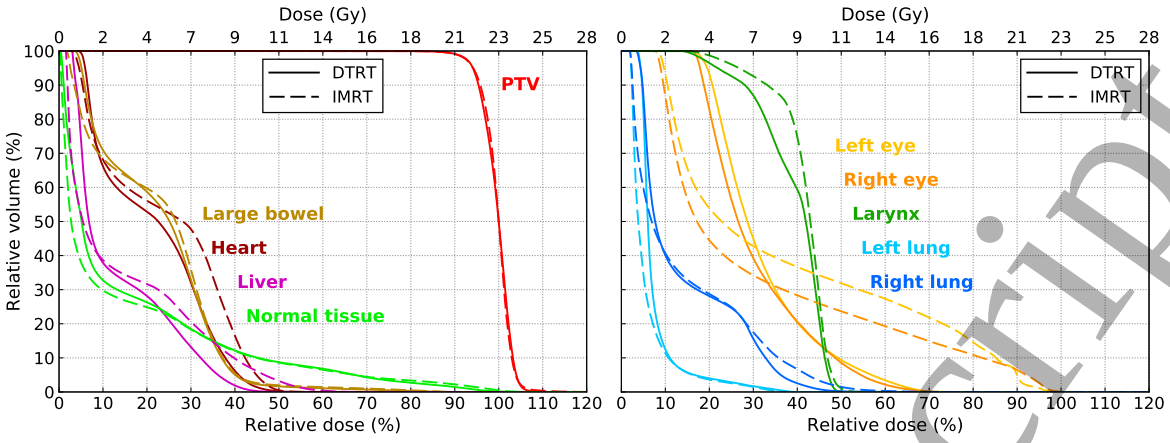

Figure 7. DVH comparison of the IMRT and the DTRT plan for the CSI case.

Table 2. Comparison of the dosimetric quantities of the IMRT and DTRT plan for the CSI case. The lower value of each quantity is highlighted in bold.

	IMRT plan	DTRT plan
PTV HI	13.8	**13.3**
Heart D_{mean} (Gy)	5.7	**5.0**
Left eye $D_{2\%}$ (Gy)	21.8	**15.2**
Right eye $D_{2\%}$ (Gy)	22.4	**15.6**
Left lung D_{mean} (Gy)	**1.3**	1.8
Right lung D_{mean} (Gy)	3.3	3.3
Left Kidney D_{mean} (Gy)	**1.3**	1.9
Right kidney D_{mean} (Gy)	**1.4**	2.0
Liver D_{mean} (Gy)	3.4	**3.1**
Large bowel D_{mean} (Gy)	**5.2**	5.3
Thyroid D_{mean} (Gy)	9.7	**9.5**
Larynx D_{mean} (Gy)	9.6	**9.1**
Normal tissue $V_{10\%}$ (%)	**29.3**	32.3

an axial plane are shown. The total MUs are 1204 for the VMAT plan and 728 for the DTRT plan. The estimated delivery times are 4.5 min for the VMAT plan and 2.4 min for the DTRT plan.

3.2. Deliverability and dosimetric validation

The DTRT plan with extended STD for the brain case and the DTRT plan for the CSI case were successfully delivered on a TrueBeam linear accelerator in developer mode without any interlocks. Videos of the deliveries are presented in the supplementary material. The passing rates of the gamma evaluation between the calculated and the

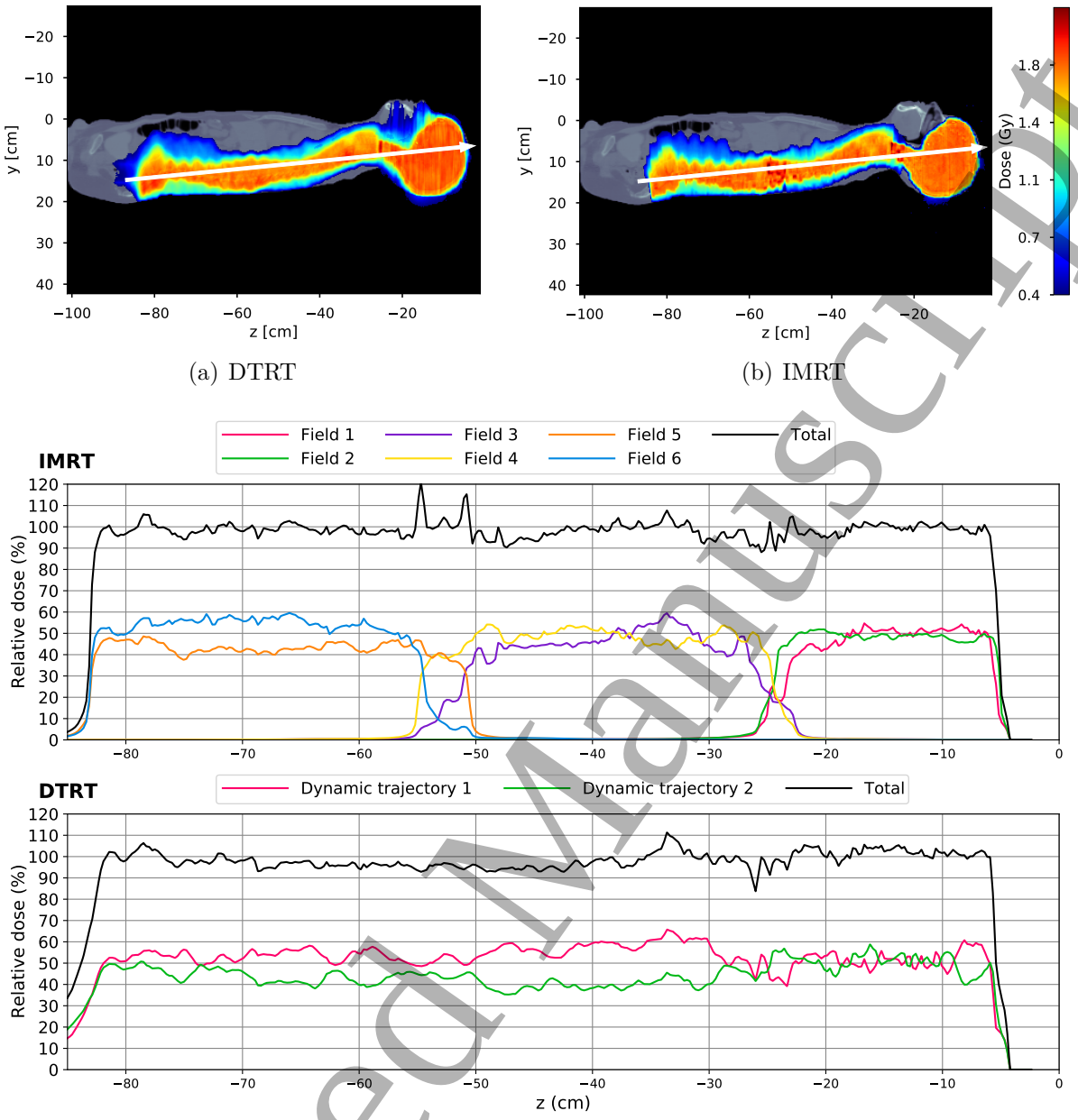

Figure 8. Dose visualization (top) of the IMRT and DTRT plans for the CSI case in a sagittal plane. Dose profiles of the IMRT plan and the DTRT plan along the white arrow are shown on the bottom.

measured doses on the EBT3 films are shown in table 3.

4. Discussion

A TPP for creating non-isocentric DTRT plans was successfully developed and a DAO algorithm for intensity modulation optimization was extended for optimizations of DTRT plans. To demonstrate a possible use case of non-isocentric DTRT, a DTRT

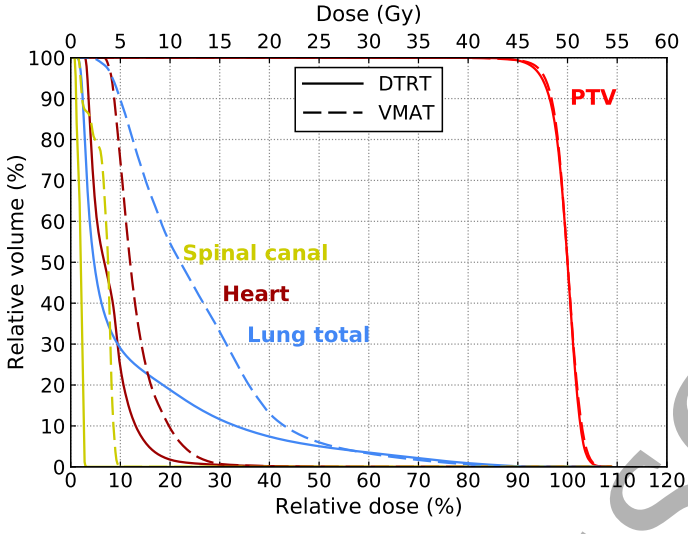

Figure 9. DVH comparison of the VMAT and DTRT plans for the WBI case.

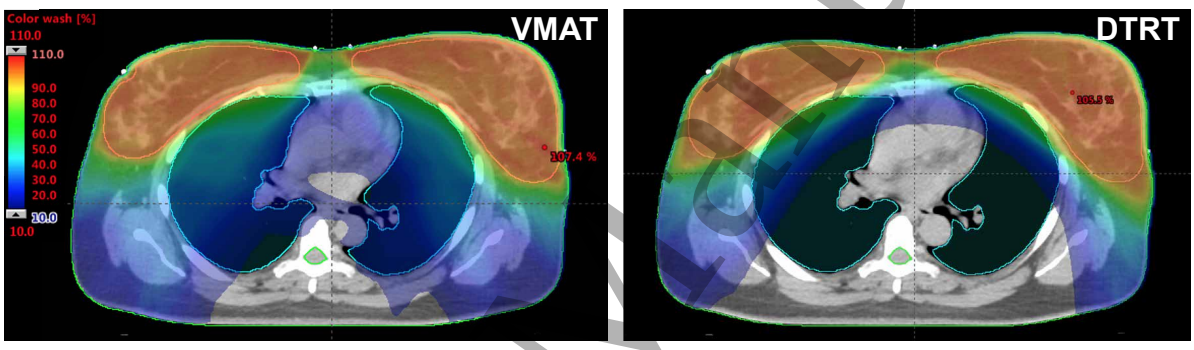

Figure 10. Dose distributions of an axial plane shown in color wash of the VMAT plan (left) and of the DTRT plan (right).

Table 3. Passing rates of gamma evaluation between measured and calculated dose distributions.

Plan	film orientation	passing rate 3%/2 mm	passing rate 2%/ 2 mm
DTRT with extended STD for brain case	sagittal	99.8%	99.1%
	coronal	99.2%	96.5%
DTRT for CSI case	sagittal	98.2%	95.6%
	coronal	97.9%	92.1%
DTRT for WBI case	axial	99.1%	97.1%
	coronal	99.2%	95.8%

plan with an extended STD of 110 cm is compared to the same DTRT plan with normal STD of 110 cm, i.e. an isocentric DTRT plan, for a brain case. The two plans show

similar dose distributions and delivery times, but extended STD is expected to reduce the risk of collision. Mullins et al. (2020a) demonstrated optimization of non-isocentric DTRT plans using a CG DAO algorithm presented by Renaud et al. (2017). In their study, DTRT plans at a shortened STD of 80 cm are compared to DTRT plans with normal STD and similar dose distributions are observed. This is consistent with our findings, even though in our case extended instead of shortened STD is investigated.

A second use case of non-isocentric DTRT is demonstrated by creating a DTRT plan for a CSI case including dynamic longitudinal table translations. Compared to the IMRT plan, the DTRT plan shows similar homogeneity in the PTV while improving the dose sparing to the heart, liver and eyes but worsening the dose to the lungs. The low dose bath is slightly higher for the DTRT plan, possibly due to the leakage through the MLC leaves inside the opened secondary collimator jaw area. A possible solution to reduce the low dose bath is enabling dynamic jaw tracking in the optimization or as a post-processing step. In the IMRT plan the jaw area is different for every field and thus less leakage through the MLC leaves occurs. Compared to the IMRT plan, the DTRT plan reduces the estimated delivery time by 45%. Another advantage of the DTRT plan is that the fields do not have field junctions as in the IMRT plan. At the field junctions, there is potential of under- or overdosage if the distance between the isocenters is not consistent (Myers et al. 2013), which makes the setup challenging. Total session time for CSI can thus take up to 20-30 min. In the DTRT plan, there are no field junctions and the plan is potentially more robust against patient setup uncertainties. Thus, the DTRT plan benefits from a simpler patient setup which reduces overall session time.

As a third use case of non-isocentric DTRT, a DTRT plan for a concave target in a bilateral WBI case is created and compared to a multi-isocentric VMAT plan. While the target coverage is maintained in the DTRT plan in comparison with the VMAT plan, the mean dose to the heart is reduced by 40% in the DTRT plan due to the more tangential beam directions in the DTRT plan, which correlates with the risk of heart disease (Darby et al. 2013). Additionally, the mean lung volume receiving 5 Gy is reduced by 67% in the DTRT plan. The delivery time is reduced by 46% in the DTRT plan in comparison with the the VMAT plan. Furthermore, the VMAT plan is a multi-isocentric setup. Because the DTRT plan covers the whole target at once, the DTRT plan might benefit from a simplified setup and thus reduced overall session time in comparison with the VMAT plan similar to the CSI case.

The three non-isocentric DTRT plans were successfully delivered in developer mode on a TrueBeam linear accelerator and the gamma passing rates of the evaluation between measured and calculated dose distributions are above 92% with 2%/2 mm criteria and above 97.9% with 3%/2 mm criteria. Thus, all passing rates are within tolerance recommended by the AAPM TG 218 (Miften et al. 2018) and validation can be judged successful. However, the topic of patient motion when the table is moved should be investigated, similar to the study of Joehl et al. (2018) for the purpose of couch tracking.

A fluence interpolation was introduced in the intensity modulation optimization to consider the dynamic movement of the MLC leaves between CPs. The effect of plan

parameters on dosimetric accuracy on calculated dose distributions for VMAT plans has been studied extensively in the past (Bedford 2009, Masi et al. 2013, Park et al. 2017). For the dose calculation of VMAT plans without fluence interpolation, a fine CP spacing has been recommended by Otto (2008) and Masi et al. (2013). However, a finer CP spacing increases the optimization computation time and beamlet dose calculation time as well as the necessary computer memory. A dose calculation for VMAT including interpolation of the MLC leaves between CPs has been proposed by Alahmad et al. (2020). However, our results show that consideration of interpolation of the MLC leaves between CPs only in the final dose calculation still leads to a large OCE. Bedford (2009), Park et al. (2017) and Christiansen et al. (2018) implemented a continuous aperture optimization for VMAT similarly to the fluence interpolation in this work. Christiansen et al. (2018) concluded that the dose prediction error due to omission of fluence interpolation is higher than the dose prediction error due to the static approximation of the CP axes in the beamlet dose calculation. Bedford et al. (2019) implemented an optimization algorithm for dynamic trajectories for Cyberknife and confirmed the findings also for dynamic trajectories. This is consistent with our results for DTRT since the DPE for optimizations with fluence interpolation is an order of magnitude lower in comparison with optimizations without fluence interpolation.

The presented two-step approach of path determination and intensity modulation optimization is beneficial in that it is straight forward to define the table translations for applications following a specific purpose or strategy such as collision avoidance. On the other side, only limited dosimetric information is considered when the paths are set up, which means the paths are potentially suboptimal. For isocentric DTRT also a one-step approach was suggested, where the gantry-table-collimator path is determined simultaneously with the intensity modulation (Dong et al. 2018, Lyu et al. 2018, Mullins et al. 2020b, MacDonald et al. 2020). However, finding an optimized path in up to six axes for non-isocentric DTRT is a difficult optimization problem and the number of CPs to be considered and consequently the number of beamlet dose calculations would rise enormously.

The beamlet dose calculations make up the bulk of the calculation time to generate a treatment plan. Including beamlet dose calculation, optimization and final dose calculation, a plan creation can take several hours. However, our beamlet dose calculation framework is currently not outlaid for high computational performance. A more sophisticated approach to reduce computation time for beamlet dose calculation is to implement a GPU-based MC dose calculation algorithm (Jia et al. 2011). More recently, deep neural networks have been used for denoising MC dose calculations (Fu et al. 2020, Bai et al. 2021, Kontaxis et al. 2020). Due to this denoising, the number of simulated particles in the MC algorithm and consequently the calculation time can be greatly reduced.

5. Conclusion

In this work, non-isocentric DTRT is enabled by integration of dynamic table translations during beam on. Three different use cases for novel non-isocentric DTRT are presented including validation of delivery and dosimetric accuracy. The demonstrated benefits of non-isocentric DTRT are versatile: reduced risk of collisions for the brain case, reduced setup and delivery time for the CSI case and improved dosimetric plan quality for the bilateral breast case.

6. Acknowledgements

This work was supported by grant 200021_185366 of the Swiss National Science Foundation and by Varian Medical Systems. Calculations are performed on ubelix, the high performance computing cluster at the University of Bern.

7. Ethical Statement

This work is part of a retrospective study with further use of health related data (Swiss Human Research Act - HRO). The study was approved by the cantonal ethics committee of Bern (project ID: 2019-01415).

References

Alahmad, H. N., Park, J. Y., Potter, N. J., Lu, B., Yan, G., Liu, C. & Li, J. G. (2020), 'A sliding-window approach for improved vmat dose calculation accuracy', *Med. Dosim.* **45**, 197–201.

Audet, C., Poffenbarger, B. A., Chang, P., Jackson, P. S., Lundahl, R. E., Ryu, S. I. & Ray, G. R. (2011), 'Evaluation of volumetric modulated arc therapy for cranial radiosurgery using multiple noncoplanar arcs', *Med. Phys.* **38**, 5863–5872.

Bai, T., Wang, B., Nguyen, D. & Jiang, S. (2021), 'Deep dose plugin: towards real-time monte carlo dose calculation through a deep learning-based denoising algorithm', *Mach. Learn.: Sci. Technol.* **2**(2), 025033.

Battinelli, C., Fredriksson, A. & Eriksson, K. (2021), 'Technical note: Collimator angle optimization for multiple brain metastases in dynamic conformal arc treatment planning', *Med. Phys.* **48**, 5414–5422.

Bedford, J. L. (2009), 'Treatment planning for volumetric modulated arc therapy', *Med. Phys.* **36**, 5128–5138.

Bedford, J. L., Lee, Y. K., Saran, F. H. & Warrington, A. P. (2012), 'Helical volumetric modulated arc therapy for treatment of craniospinal axis', *Int. J. Rad. Biol. Phys.* **83**(3), 1047–1054.

Bedford, J. L., Tsang, H. S., Nill, S. & Oelfke, U. (2019), 'Treatment planning optimization with beam motion modeling for dynamic arc delivery of sbrt using cyberknife with multileaf collimation', *Med. Phys.* **46**, 5421–5433.

Bortfeld, T. (2006), 'Imrt: a review and preview', *Phys. Med. Biol.* **51**, R363.

Christiansen, E., Heath, E. & Xu, T. (2018), 'Continuous aperture dose calculation and optimization for volumetric modulated arc therapy', *Phys. Med. Biol.* **63**.

Clark, G. M., Popple, R. A., Prendergast, B. M., Spencer, S. A., Thomas, E. M., Stewart, J. G., Guthrie, B. L., Markert, J. M. & Fiveash, J. B. (2012), 'Plan quality and treatment planning technique for single isocenter cranial radiosurgery with volumetric modulated arc therapy', *Pract. Radiat. Oncol.* **2**, 306–313.

Darby, S. C., Ewertz, M., McGale, P., Bennet, A. M., Blom-Goldman, U., BrÃÿnnum, D., Correa, C., Cutter, D., Gagliardi, G., Gigante, B., Jensen, M.-B., Nisbet, A., Peto, R., Rahimi, K., Taylor, C. & Hall, P. (2013), 'Risk of ischemic heart disease in women after radiotherapy for breast cancer', *N. Engl. J. Med.* **368**(11), 987–998.

Dong, P., Lee, P., Ruan, D., Long, T., Romeijn, E., Yang, Y., Low, D., Kupelian, P. & Sheng, K. (2013), '4π non-coplanar liver sbrt: A novel delivery technique', *Int. J. Radiat. Oncol. Biol. Phys.* **85**, 1360–1366.

Dong, P., Liu, H. & Xing, L. (2018), 'Monte carlo tree search -based non-coplanar trajectory design for station parameter optimized radiation therapy (sport)', *Phys. Med. Biol.* **63**, 135014.

Fix, M. K., Frei, D., Volken, W., Terribilini, D., Mueller, S., Elicin, O., Hemmatazad, H., Aebersold, D. M. & Manser, P. (2018), 'Part 1: Optimization and evaluation of dynamic trajectory radiotherapy', *Med. Phys.* **45**, 4201–4212.

Fix, M. K., Manser, P., Frei, D., Volken, W., Mini, R. & Born, E. J. (2007), 'An efficient framework for photon monte carlo treatment planning', *Phys. Med. Biol.* **52**, N425.

Fu, J., Bai, J., Liu, Y. & Ni, C. (2020), 'Fast monte carlo dose calculation based on deep learning', *Proc. - 2020 13th Int. Congr. Image Signal Process. BioMed. Eng. Inform. CISP-BMEI* pp. 721–726.

Hart, P. E., Nilsson, N. J. & Raphael, B. (1968), 'A formal basis for the heuristic determination of minimum cost paths', *EEE Trans. Syst. Sci. Cybern.* **4**(2), 100–107.

Humm, J. L. (1994), 'Collision avoidance in computer optimized treatment planning', *Med. Phys.* **21**(7), 1053–1064.

Jia, X., Gu, X., Graves, Y. J., Folkerts, M. & Jiang, S. B. (2011), 'Gpu-based fast monte carlo simulation for radiotherapy dose calculation', *Phys. Med. Biol.* **56**.

Joehl, A., Bogowicz, M., Ehrbar, S., Guckenberger, M., Kloeck, S., Meboldt, M., Riesterer, O., Zeilinger, M., Daners, M. S. & Tanadini-Lang, S. (2018), 'Body motion during dynamic couch tracking with healthy volunteers', *Phys. Med. Biol.* **64**(1), 015001.

Kawrakow, I. & Fippel, M. (2000), 'Vmc++, a fast mc algorithm for radiation treatment planning', *Use Comput. Radiat. Ther. 8th Int. Conf. (Heidelberg, Ger.) ed W Schlegel T Bortfeld (Heidelberg Springer)* pp. 126–128.

Kontaxis, C., Bol, G. H., Lagendijk, J. J. W. & Raaymakers, B. W. (2020), 'Deepdose: Towards a fast dose calculation engine for radiation therapy using deep learning', *Phys. Med. Biol.* **65**(7), 075013.

Langhans, M., Unkelbach, J., Bortfeld, T. & Craft, D. (2018), 'Optimizing highly noncoplanar vmat trajectories: the novo method', *Phys. Med. Biol.* **63**, 025023.

Laprie, A., Hu, Y., Alapetite, C., Carrie, C., Habrand, J.-L., Bolle, S., Bondiau, P.-Y., Ducassou, A., Huchet, A., Bertozzi, A.-I., Perel, Y., Moyal, E. & Balosso, J. (2015), 'Paediatric brain tumours: A review of radiotherapy, state of the art and challenges for the future regarding protontherapy and carbontherapy', *Cancer Radiother.* **19**(8), 775–789.

Lewis, D. & Chan, M. F. (2015), 'Correcting lateral response artifacts from flatbed scanners for radiochromic film dosimetry', *Med. Phys.* **42**, 416–429.

Lewis, D., Micke, A., Yu, X. & Chan, M. F. (2012), 'An efficient protocol for radiochromic film dosimetry combining calibration and measurement in a single scan', *Med. Phys.* **39**, 6339–6350.

Li, R., Xing, L., Horst, K. C. & Bush, K. (2014), 'Nonisocentric treatment strategy for breast radiation therapy: A proof of concept study', *Int. J. Radiat. Oncol. Biol. Phys.* **88**, 920–926.

Liang, J., Atwood, T., Eyben, R. V., Fahimian, B., Chin, E., Horst, K., Otto, K. & Hristov, D. (2015), 'Trajectory modulated arc therapy: A fully dynamic delivery with synchronized couch and gantry motion significantly improves dosimetric indices correlated with poor cosmesis in accelerated partial breast irradiation', *Int. J. Radiat. Oncol. Biol. Phys.* **92**, 1148–1156.

Locke, C. B. & Bush, K. K. (2017), 'Trajectory optimization in radiotherapy using sectioning (torus)', *Med. Phys.* **44**, 3375–3392.

Lyu, Q., Yu, V. Y., Ruan, D., Neph, R., O'Connor, D. & Sheng, K. (2018), 'A novel optimization framework for vmat with dynamic gantry couch rotation', *Phys. Med. Biol.* **63**.

MacDonald, R. L., Syme, A., Little, B., Ward, L. & Thomas, C. G. (2020), 'Toward the combined optimization of dynamic axes (coda) for stereotactic radiotherapy and radiosurgery using fixed couch trajectories', *Med. Phys.* **47**, 307–316.

MacDonald, R. L. & Thomas, C. G. (2015), 'Dynamic trajectory-based couch motion for improvement of radiation therapy trajectories in cranial srt', *Med. Phys.* **42**, 2317–2325.

MacDonald, R. L., Thomas, C. G. & Syme, A. (2018), 'Dynamic collimator trajectory algorithm for multiple metastases dynamic conformal arc treatment planning', *Medical Physics* **45**(1), 5–17.

Magaddino, V., Manser, P., Frei, D., Volken, W., Schmidhalter, D., Hirschi, L. & Fix, M. K. (2011), 'Validation of the swiss monte carlo plan for a static and dynamic 6 mv photon beam', *Z. Med. Phys.* **21**, 124–134.

Maillie, L., Salgado, L. R. & Lazarev, S. (2021), 'A systematic review of craniospinal irradiation for leptomeningeal disease: past, present, and future', *Clin. Transl. Oncol.* **23**, 2109–2119.

Manser, P., Frauchiger, D., Frei, D., Volken, W., Terribilini, D. & Fix, M. K. (2019), 'Dose calculation of dynamic trajectory radiotherapy using monte carlo', *Z. Med. Phys.* **29**, 31–38.

Manser, P., Mueller, S., Guyer, G., Koechli, C., Volken, W., Bertholet, J., Aebersold, D. M. & Fix, M. K. (2020), 'Advanced dynamic trajectory radiotherapy using table translations and rotations', *Int. J. Radiat. Oncol. Biol. Phys.* **108**(3), e335.

Masi, L., Doro, R., Favuzza, V., Cipressi, S. & Livi, L. (2013), 'Impact of plan parameters on the dosimetric accuracy of volumetric modulated arc therapy', *Med. Phys.* **40**.

Massimino, M., Biassoni, V., Gandola, L., Garrè, M. L., Gatta, G., Giangaspero, F., Poggi, G. & Rutkowski, S. (2016), 'Childhood medulloblastoma', *Crit. Rev. Oncol. Hematol.* **105**, 35–51.

Micke, A., Lewis, D. F. & Yu, X. (2011), 'Multichannel film dosimetry with nonuniformity correction', *Med. Phys.* **38**, 2523–2534.

Miften, M., Olch, A., Mihailidis, D., Moran, J., Pawlicki, T., Molineu, A., Li, H., Wijesooriya, K., Shi, J., Xia, P., Papanikolaou, N. & Low, D. A. (2018), 'Tolerance limits and methodologies for imrt measurement-based verification qa: Recommendations of aapm task group no. 218', *Med. Phys.* **45**, e53–e83.

Mueller, S., Guyer, G., Risse, T., Tessarini, S., Aebersold, D. M., Stampanoni, M. F. M., Fix, M. K. & Manser, P. (2022), 'A hybrid column generation and simulated annealing algorithm for direct aperture optimization', *Phys. Med. Biol.* **67**(7), 075003.

Mullins, J., Renaud, M. A., Heng, V., Ruo, R., DeBlois, F. & Seuntjens, J. (2020a), 'Trajectory-based vmat for cranial targets with delivery at shortened sad', *Med. Phys.* **47**, 3103–3112.

Mullins, J., Renaud, M. A., Serban, M. & Seuntjens, J. (2020b), 'Simultaneous trajectory generation and volumetric modulated arc therapy optimization', *Med. Phys.* **47**, 3078–3090.

Nocedal, J. & Wright, S. J. (1999), *Numerical Optimization*, second edn, Springer, New York, NY, USA.

Otto, K. (2008), 'Volumetric modulated arc therapy: Imrt in a single gantry arc', *Med. Phys.* **35**, 310–317.

Papp, D., Bortfeld, T. & Unkelbach, J. (2015), 'A modular approach to intensity-modulated arc therapy optimization with noncoplanar trajectories', *Phys. Med. Biol.* **60**, 5179–5198.

Park, J. Y., Li, F., Li, J., Kahler, D., Park, J. C., Yan, G., Liu, C. & Lu, B. (2017), 'Angular under-sampling effect on vmat dose calculation: An analysis and a solution strategy', *Med. Phys.* **44**, 2096–2114.

Renaud, M. A., Serban, M. & Seuntjens, J. (2017), 'On mixed electron-photon radiation therapy optimization using the column generation approach', *Med. Phys.* **44**, 4287–4298.

Rwigema, J.-C. M., Nguyen, D., Heron, D. E., Chen, A. M., Lee, P., Wang, P.-C., Vargo, J. A., Low, D. A., Huq, M. S., Tenn, S., Steinberg, M. L., Kupelian, P. & Sheng, K. (2015), '4π noncoplanar stereotactic body radiation therapy for head-and-neck cancer: Potential to improve tumor control and late toxicity', *Int. J. Radiat. Oncol. Biol. Phys.* **91**, 401–409.

Schmidhalter, D., Malthaner, M., Born, E. J., Pica, A., Schmuecking, M., Aebersold, D. M., Fix, M. K. & Manser, P. (2014), 'Assessment of patient setup errors in igrt in combination with a six degrees of freedom couch', *Z. Med. Phys.* **24**(2), 112–122.

Seravalli, E., Bosman, M., Lassen-Ramshad, Y., Vestergaard, A., Oldenburger, F., Visser, J., Koutsouveli, E., Paraskevopoulou, C., Horan, G., Ajithkumar, T., Timmermann, B., Fuentes, C. S., Whitfield, G., Marchant, T., Padovani, L., Garnier, E., Gandola, L., Meroni, S., Hoeben, B. A., Kusters, M., Alapetite, C., Losa, S., Goudjil, F., Magelssen, H., Evensen, M. E., Saran, F., Smyth, G., Rombi, B., Righetto, R., Kortmann, R. D. & Janssens, G. O. (2018), 'Dosimetric comparison of five different techniques for craniospinal irradiation across 15 european centers: analysis on behalf of the siop-e-btg (radiotherapy working group)*', *Acta Oncol.* **57**, 1240–1249.

Smyth, G., Bamber, J. C., Evans, P. M. & Bedford, J. L. (2013), 'Trajectory optimization for dynamic couch rotation during volumetric modulated arc radiotherapy', *Phys. Med. Biol.* **58**, 8163.

Smyth, G., Evans, P. M., Bamber, J. C. & Bedford, J. L. (2019b), 'Recent developments in non-coplanar radiotherapy', *Br. J. Radiol. Suppl.* **92**.

Smyth, G., Evans, P. M., Bamber, J. C., Mandeville, H. C., Moore, A. R., Welsh, L. C., Saran, F. H. & Bedford, J. L. (2019a), 'Dosimetric accuracy of dynamic couch rotation during volumetric modulated arc therapy (dcr-vmat) for primary brain tumours', *Phys. Med. Biol.* **64**.

Wild, E., Bangert, M., Nill, S. & Oelfke, U. (2015), 'Noncoplanar vmat for nasopharyngeal tumors: Plan quality versus treatment time', *Med. Phys.* **42**, 2157–2168.

Yang, Y., Zhang, P., Happersett, L., Xiong, J., Yang, J., Chan, M., Beal, K., Mageras, G. & Hunt, M. (2011), 'Choreographing couch and collimator in volumetric modulated arc therapy', *Int. J. Radiat. Oncol. Biol. Phys.* **80**, 1238–1247.

Yu, V. Y., Landers, A., Woods, K., Nguyen, D., Cao, M., Du, D., Chin, R. K., Sheng, K. & Kaprealian, T. B. (2018), 'A prospective 4π radiation therapy clinical study in recurrent high-grade glioma patients', *Int. J. Radiat. Oncol. Biol. Phys.* **101**, 144–151.

Yu, V. Y., Tran, A., Nguyen, D., Cao, M., Ruan, D., Low, D. A. & Sheng, K. (2015), 'The development and verification of a highly accurate collision prediction model for automated noncoplanar plan delivery', *Med. Phys.* **42**, 6457–6467.

Appendix A. Calculation of fluence considering neighbor interpolation

In the following, the formalism of calculating the fluence considering interpolation to the neighboring apertures for one MLC leaf pair j is described.

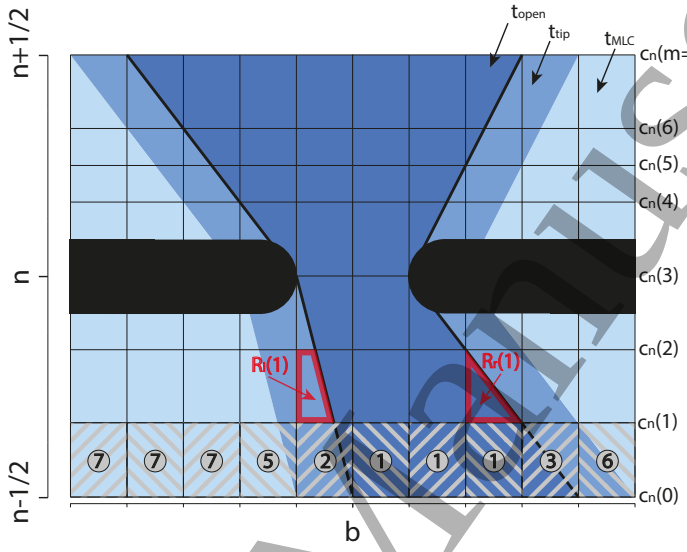

Figure A1. Illustration of the fluence calculation for one leaf pair at the nth CP. The interpolated leaves move from $n-1/2$ to $n+1/2$. The tips of either the left or the right leaf cross beamlet boundaries in the leaf direction at the positions $c_n(0),\ldots,c_n(7)$ along the CP direction including start and endpoint. Between positions $c_n(0)$ and $c_n(1)$ the case which each beamlet occupies in (A.3) is visualized with the number in each section corresponding to the case number in (A.3). Between positions $c_n(1)$ and $c_n(2)$ the area of the trapezoids $R_l(1)$ and $R_r(1)$ are highlighted, which are used for the fluence calculation in (A.3). The transmission factors t_{open}, t_{tip} and t_{MLC} are used in the fluence calculation to approximate the leakage through the MLC leaves and ar illustrated in different colors.

Let $l_j(n)$ be the position of the left leaf and $r_j(n)$ be the position of the right leaf of the MLC leaf pair j at the nth CP. The fluence of the aperture at the nth CP takes the interpolated leaf positions between $n-1/2$ to $n+1/2$ into account. The leaf positions at $n-1/2$ are calculated using linear interpolation to the next preceding active CP

$$l_j(n-1/2) = \big(1/(2\cdot q)\big)\cdot l_j(n-q) + \big(1-1/(2\cdot q)\big)\cdot l_j(n) \qquad \text{(A.1)}$$

$$r_j(n-1/2) = \big(1/(2\cdot q)\big)\cdot r_j(n-q) + \big(1-1/(2\cdot q)\big)\cdot r_j(n), \qquad \text{(A.2)}$$

with q CPs between the two apertures. The leaf positions at $n+1/2$ are calculated analogously using linear interpolation to the next succeeding active CP. To calculate the fluence $\phi_n(b,j)$ per beamlet b of the leaf pair j, let $l_j(y)$ and $r_j(y)$ be the linearly

interpolated functions of leaf positions with continuous CP position y between $n-1/2$, n and $n+1/2$. Let c_n: $[0,1,\ldots,m] \to [n-1/2, n+1/2]$ be the function of positions in the CP direction where either $l_j(y)$ or $r_j(y)$ crosses a beamlet border in the leaf direction with $c_n(0) = n-1/2$ and $c_n(m) = n+1/2$ where m is the number of crossings. Start and end point are included as a crossing regardless of position. With this formalism, the fluence can be split up into $k = 0,\ldots,m-1$ fluence sections and calculated in the following way:

$$\phi_n(b,j,k) = \begin{cases} t_{open}\cdot(c_n(k+1)-c_n(k)) & 1)\ \text{if } b_l(k) < b < b_r(k) \\ t_{open}\cdot(1-R_l(k)) + t_{tip}\cdot R_l(k) & 2)\ \text{if } b_l(k) = b \text{ and } b < b_r(k) \\ t_{open}\cdot R_r(k) + t_{tip}\cdot(1-R_r(k)) & 3)\ \text{if } b_l(k) < b \text{ and } b = b_r(k) \\ t_{open}\cdot(R_r(k)-R_l(k)) + t_{tip}\cdot(1-R_r(k)+R_l(k)) & 4)\ \text{if } b_l(k) = b \text{ and } b = b_r(k) \\ t_{tip}\cdot(1-R_l(k)) + t_{MLC}\cdot R_l(k) & 5)\ \text{if } b_l(k)-1 = b \\ t_{tip}\cdot R_r(k) + t_{MLC}\cdot(1-R_r(k)) & 6)\ \text{if } b = 1+b_r(k) \\ t_{MLC}\cdot(c_n(k+1)-c_n(k)) & 7)\ \text{else} \end{cases} \quad \text{(A.3)}$$

This is illustrated in figure A1. $R_l(k)$ and $R_r(k)$ correspond to the area of the trapezoid shown in the figure and are calculated as follows.

$$R_l(k) = \Big(\frac{1}{2}l_j(c_n(k+1)) + \frac{1}{2}l_j(c_n(k)) - b_l(k)\Big)\cdot\Big(c_n(k+1)-c_n(k)\Big) \quad \text{(A.4)}$$

$$R_r(k) = \Big(\frac{1}{2}r_j(c_n(k+1)) + \frac{1}{2}r_j(c_n(k)) - b_r(k)\Big)\cdot\Big(c_n(k+1)-c_n(k)\Big) \quad \text{(A.5)}$$

$b_l(k)$ and $b_r(k)$ refers to the beamlet, where the left and right leaf tip lies within k and $k+1$, respectively. To consider the leakage through the MLC leaves, three transmission factors $(t_{open}, t_{tip}, t_{MLC})$ are defined, corresponding to no cover with an MLC leaf, cover with the MLC tip and cover with the rest of the MLC leaf. The values for the transmission factors were determined for a specific TrueBeam linear accelerator equipped with a Millennium 120 MLC (Varian Medical Systems, Palo Alto, USA) and are $1, 0.129, 0.013$ for $t_{open}, t_{tip}, t_{MLC}$, respectively. The fluence $\phi_n(b,j)$ is now calculated by summing over k

$$\phi_n(b,j) = \sum_{k=0}^{m-1} \phi_n(b,j,k). \quad \text{(A.6)}$$

Appendix B. Optimization efficacy

To evaluate the efficacy of the optimization algorithm, a VMAT setup for a unilateral head and neck (H&N) case and the non-isocentric DTRT setup for the CSI case are considered.

The VMAT field setup consists of two arcs for the H&N case with a prescribed dose of 50 Gy to D_{95} of the PTV in 25 fractions. The spacing between CPs is 5° in gantry angle. Treatment plans for the H&N case are created using the following parameters for the optimization of the intensity modulation:

Table B1. Results of the VMAT plans for the H&N case with and without interpolation used during optimization.

	with fluence interpolation				without fluence interpolation				IMRT
λ_{MU} — λ_{MLC}	1 — 1	1 — ∞	∞ — 1	∞ — ∞	1 — 1	1 — ∞	∞ — 1	∞ — ∞	
Optimization time (min)	31.1	26.6	31.9	28.5	21.0	22.1	25.8	18.3	23.7
Total MUs	579.5	640.6	756.7	824.8	610.7	700.9	772.3	850.9	839.8
Obj. fct. after optim. f_O	1.7	1.2	1.1	0.9	1.2	0.7	0.8	0.6	0.5
Obj. fct. after final dose calc. f_F	13.3	6.0	3.5	2.7	18.7	146.2	10.9	176.0	1.9
Obj. fct. after reoptim. f_R	2.6	2.0	2.0	1.8	3.2	8.9	4.5	11.4	1.4
PTV HI	14.9	14.3	14.5	14.3	17.5	25.6	21.3	28.2	14.1
Estimated delivery time (min)	2.0	6.8	2.4	6.9	2.0	6.6	2.4	6.7	9.2

(i) Fluence interpolation: yes, no

(ii) MLC freedom factor λ_{MLC}: 1, ∞

(iii) MU freedom factor λ_{MU}: 1, ∞

Additionally, an IMRT plan is created with the fields given by the CPs of the paths, where the maximal number of apertures is the same as the number of CPs. Thus, the number of apertures in the IMRT plan are the same as the number of apertures in the VMAT plans with the possibility of multiple apertures at one CP.

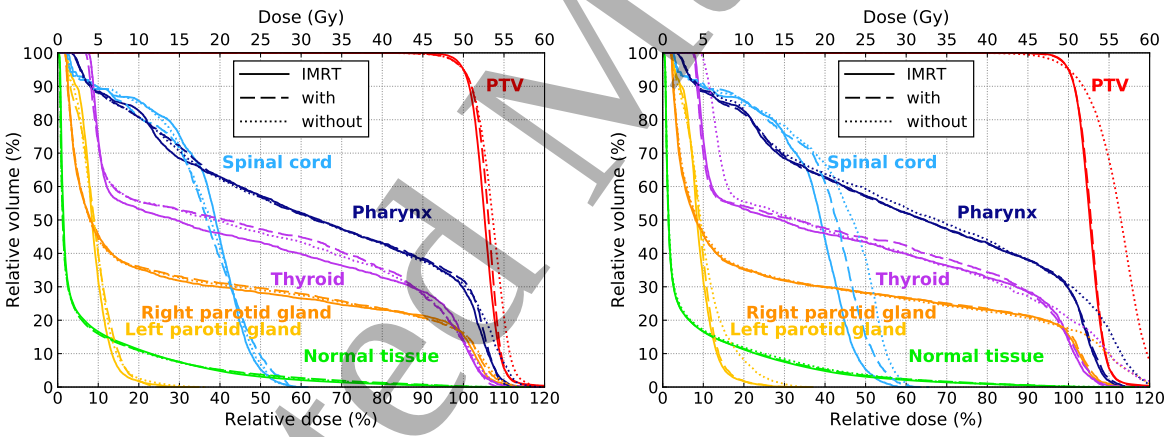

(a) $\lambda_{MU} = 1$ and $\lambda_{MLC} = 1$ (b) $\lambda_{MU} = \infty$ and $\lambda_{MLC} = \infty$

Figure B1. DVH comparison of plans with and without consideration of fluence interpolation and the benchmark IMRT plan for the H&N case after the final dose calculation and MU weight reoptimization.

In table B1 the objective function values after the optimization f_O, after the final dose calculation f_F and after the reoptimization f_R of the VMAT plans for the H&N case are shown. As can be seen, there is a much greater difference between f_O, f_F and f_R without fluence interpolation than with fluence interpolation. Figure B1 shows the dosimetric differences between optimizations performed with and without fluence interpolation for the two extreme settings of $\lambda_{MU} = 1$, $\lambda_{MLC} = 1$ and $\lambda_{MU} = \infty$,

$\lambda_{MLC} = \infty$ of the VMAT plan and the benchmark IMRT plan. It is visible that while the PTV homogeneity and doses to OARs decrease with increasing freedom for the plans with fluence interpolation, the PTV homogeneity and maximum doses to OARs increase with increasing freedom for the plans without fluence interpolation. Thus, optimizations without fluence interpolation show inaccuracies in dose prediction, which cannot be accounted for with the MU weight reoptimization. The plans with fluence interpolation are similar to the benchmark IMRT plan.

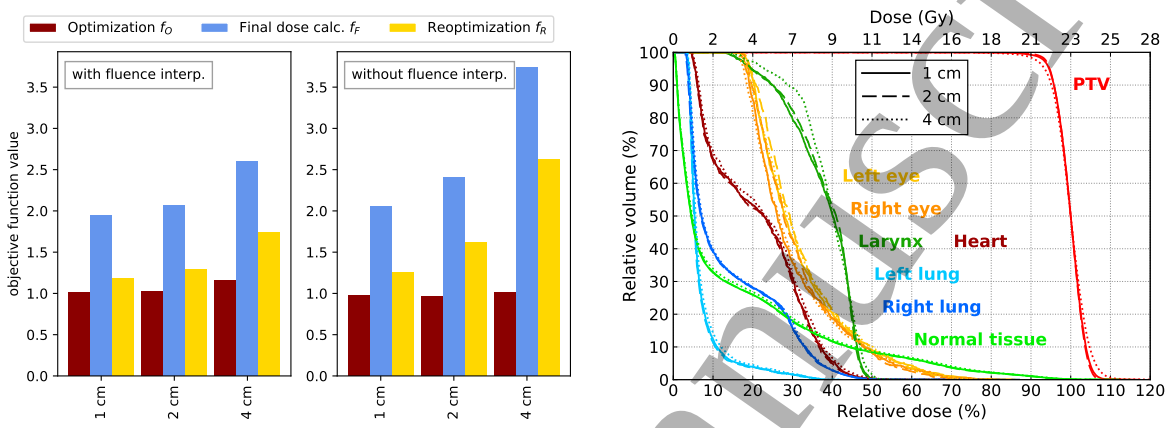

(a) Objective function values (b) DVH

Figure B2. a) Objective function values after the optimization f_O, after the final dose calculation f_F and after the reoptimization f_R of the DTRT plans for the CSI case with CP spacing along the longitudinal axis set to 1 cm, 2 cm and 4 cm and with and without fluence interpolation applied. b) DVHs of the final DTRT plans with fluence interpolation for CP spacing of 1 cm, 2 cm and 4 cm.

The DTRT setup for the CSI case is the same as in 2.2 with the spacing of CPs set to 5° along the gantry direction, $\lambda_{MU} = 2$ and $\lambda_{MLC} = 1$. For the spacing along the longitudinal table axis and fluence interpolation, following parameters are used:

(i) Fluence interpolation: yes, no

(ii) CP spacing in longitudinal direction: 1 cm, 2 cm and 4 cm

In figure B2(a) the objective function values after the optimization f_O, after the final dose calculation f_F and after the reoptimization f_R of the DTRT plans for the CSI case are shown. The values are similar for a spacing of 1 cm with and without fluence interpolation but diverge increasingly for 2 cm and 4 cm without fluence interpolation. In figure B2(b), the DVHs of the final DTRT plans with fluence interpolation for 1, 2 and 4 cm spacing are shown. As can be seen, the DVHs of the plans with 1 cm and 2 cm are similar, while for 4 cm the dose homogeneity in the PTV is lower and the dose to the larynx is higher. Thus, a spacing of 2 cm in table translation provides similar results to a 1 cm spacing for optimizations with fluence interpolation, but optimizations with a coarser spacing are not able to accurately predict the dose for the investigated CSI case.